

# Modelling the anisotropic fracture behaviour of cold spray additive manufactured 6061 aluminium alloy deposits based on the phase field method

Xuanyu Ge<sup>a</sup>, Yu'e Ma<sup>a,\*</sup>, Linglong Zhou<sup>a</sup>, Wenya Li<sup>b</sup>

<sup>a</sup> School of Aeronautics, Northwestern Polytechnical University, Xi'an 710072, Shaanxi, China

<sup>b</sup> State Key Laboratory of Solidification Processing, Shaanxi Key Laboratory of Friction Welding Technologies, Northwestern Polytechnical University, Xi'an 710072, Shaanxi, China



## ARTICLE INFO

### Keywords:

Cold spray additive manufacturing  
Particle impact  
Phase field method  
Image recognition  
Anisotropic fracture behaviour

## ABSTRACT

Cold spraying has been widely accepted as a promising additive manufacturing technique to produce large metallic structures. The fracture behaviour of cold spray additive manufactured deposits is complex because of their inherent anisotropy. In order to study the anisotropic fracture, a multiple-particle impacting model was established in a Lagrangian frame. Then, an image recognition program was developed to convert the simulated deposit image into a finite element discretisation scheme. In finite element framework, a phase field model was proposed to simulate the fracture process of deposits under tensile loading along (0°) and perpendicular (90°) to the particle impacting direction. The deposit anisotropic fracture behaviour for two impact velocities, at 600 m/s and 800 m/s, was investigated. It is shown that the interfacial fracture toughness is the most important parameter that affects the tensile properties of deposits. The tensile ultimate load of the deposit increases thrice when the interfacial fracture toughness increases by an order of magnitude. For the 800 m/s deposit, the ultimate load and fatigue life in 90° loading direction are about 11.3% and 39.2% higher than those in 0° loading direction, respectively. The fracture anisotropy relates to the degree of flattening of the deformed particles. The higher interfacial fracture toughness of mode II can lead to more transparticular cracks, shorter crack length and smoother crack path. The comparison between simulations and published experimental results suggests that the proposed phase field model can capture the complex anisotropic fracture behaviour of cold sprayed deposits.

## 1. Introduction

Cold spraying is a solid-state coating deposition process, which is being used in a wide range of applications, from surface protection to repair of metal parts. Several years ago, it was also identified as an additive manufacturing technique, i.e. cold spray additive manufacturing (CSAM) [1–3]. During deposition process, micron-sized metal particles are accelerated to high velocities by a compressed gas, and then they impact a substrate to form a coating [4–6]. It is different from the conventional thermal spraying, the particle temperature during cold spraying is lower than its melting point. Bonding at the substrate-particle or particle-particle interface is believed to be the following reason: the interface-instability-induced physical anchoring effect, the partial melting of metal and the fracture of particle surface oxide [5]. The adiabatic shear instability will cause the metallurgical

bonding due to explosive cladding [7]. As particle impact velocity increases, the bonding mechanism transforms from mechanical interlocking to metallurgical bonding [8], which improves bonding properties. Parameters such as particle temperature, particle size, particle and substrate materials properties are the other factors that affect the bonding quality [9]. Also, impact velocity affects the degree of particles flattening [10]. For the CSAMed deposits, cracks generally initiate at the weak bonding interfaces between the deformed particles [11], producing very low ductility and premature fracture of deposits. The degree of particles flattening affects crack paths in different loading directions, which leads to the anisotropic fracture behaviour of deposits [9].

Many studies about the mechanical properties of CSAMed deposits have been published [12–22], with limited number of reports on the anisotropic fracture behaviour. Julien et al. [23] measured the fracture

\* Correspondence to: Institute of Structure Integrity Analysis, Northwestern Polytechnical University.

E-mail addresses: [275216366@qq.com](mailto:275216366@qq.com) (X. Ge), [ma.yu.e@nwpu.edu.cn](mailto:ma.yu.e@nwpu.edu.cn) (Y. Ma), [xplane@126.com](mailto:xplane@126.com) (L. Zhou), [liwy@nwpu.edu.cn](mailto:liwy@nwpu.edu.cn) (W. Li).

toughness of 6061 Al deposits in three directions and found the fracture toughness of out-of-plane crack propagation is slightly higher than that of in-plane crack propagation. Ren et al. [24] investigated the in-plane and three-dimensional fracture anisotropy of 7075 Al deposits. They found that when the loading direction is perpendicular to the particle impacting direction, the ultimate load of deposits is the lowest. Yin et al. [25] investigated the fracture anisotropy of Cu deposits, and measured bonding properties and fracture modes in different tensile directions due to the fracture anisotropy. Yang et al. [26] measured the tensile properties of Cu deposits in six directions and found that the deposits reach the largest ultimate tensile strength and elongation in loading direction of 15°–30°. In order to investigate in detail the anisotropic fracture behaviour of CSAMed deposits, the whole process from the deposition process to the crack initiation and propagation should be considered.

In recent years, many numerical methods such as the Lagrangian method [27], the Eulerian method [28], the Molecular Dynamics (MD) method [29] and the Peridynamics (PD) method [30] have been used to simulate the cold spraying deposition process. The Lagrangian method is more efficient, but severe distortion of the mesh will cause the convergence problem in high impact velocity. The Eulerian method can overcome the elemental distortion but it needs more computational time due to the fine mesh. The MD method is similar to PD method, they can be used to study the microscopic mechanisms in deposition process. However, they generally need high calculation cost and the simulation results are hard to combine with other finite element methods. Among these numerical methods, only the Lagrangian method can be used to calculate the clear boundaries of deposits. Based on it, Assadi et al. [7] simulated the deposition behaviour of Cu particles and calculated the critical velocity. Bae et al. [31] investigated the bonding characteristics of pure titanium coatings. Vinay et al. [32,33] studied the bonding properties of deposits produced at different velocities and temperatures. Kumar et al. [9] proposed a systematic approach to estimate the inter-splat bonding state at splat boundaries.

The authors think that the phase field method (PFM) is appropriate for simulating the fracture process of CSAMed deposits due to its superior properties in solving complex and arbitrary crack paths [34]. It has been applied in many fields, such as ductile fracture [35], fatigue damage [36], hydrogen embrittlement [37] and composites [38]. The PFM originated from the fracture variational method proposed by Francfort and Marigo [39], as an extension of the classical Griffith's theory [40]. In the PFM framework, the continuously varying damage parameter is introduced to approximate the sharp crack discontinuity. The fracture problem can be regarded as the energy minimum problem by solving the phase field governing equation. By solving the partial differential equation of PFM, crack growth can be naturally tracked. Thus, the complex fracture behaviour such as crack nucleation, initiation, propagation, branching and merging can be solved by the PFM [41]. Cracks in a deposit may change their propagating direction as particles become flattened after spraying on the substrate, and cracks may propagate in a mixed mode of interparticular and transparticular. It is very difficult to simulate this complex anisotropic fracture behaviour with traditional fracture methods. Therefore, it is necessary to establish a phase field model for CSAMed deposits.

In this study, a phase field model was proposed to simulate the crack growth of CSAMed deposits. Deposition processes with two different impact velocities were simulated using the Lagrangian method. Then, the crack path and the load-displacement curve of deposits in different loading directions were calculated. The different interfacial fracture toughnesses were set to investigate the effect of bonding properties on the fracture behaviour. Finally, the crack initiation and propagation of deposits under fatigue loading were also simulated. The anisotropic fracture behaviour of CSAMed deposits significantly affects the application of this technology. The proposed model can not only help us better understand the fracture mechanism of deposits, but also be used to predict the fracture behaviour of deposits.

## 2. Phase field model for CSAMed deposits

In this section, the basic equations of phase field method were introduced. And then the governing equations was modified, the phase field model used for simulating the anisotropic fracture behaviour of CSAMed deposits was established.

### 2.1. Constitutive theory

Based on the variational approach [39], the internal potential energy  $W_{\text{int}}$  of the domain  $\Omega$  is expressed as:

$$W_{\text{int}} = \int_{\Omega/\Gamma} \psi(\epsilon) d\Omega + \int_{\Gamma} G_c d\Gamma \quad (1)$$

where  $G_c$  is the critical energy release rate,  $\Gamma$  is the discrete crack surface,  $\epsilon$  is the strain and  $\psi(\epsilon)$  is the strain energy density. The phase field parameter  $\phi$  was introduced to numerically track the discrete crack surface, and it varies between the sound material ( $\phi = 0$ ) and the broken material ( $\phi = 1$ ). The widely used degradation function  $g(\phi) = (1 - \phi)^2$  was introduced, and the AT2 model [42] was used. Then, the internal potential energy  $W_{\text{int}}$  can be formulated as:

$$W_{\text{int}} = \int_{\Omega} (1 - \phi)^2 \psi_0(\epsilon) d\Omega + \int_{\Omega} \frac{G_c}{2} \left( \frac{\phi^2}{l} + l |\nabla \phi|^2 \right) d\Omega \quad (2)$$

where  $l$  is the regularization length and  $\psi_0(\epsilon)$  is the undamaged strain energy. Only the tensile deformation energy is degraded to prevent cracking under compressive loading. The strain energy density is expressed as:

$$\psi(\epsilon) = (1 - \phi)^2 \psi_0^+(\epsilon) + \psi_0^-(\epsilon) \quad (3)$$

The hybrid formulation [43] was used to improve the robustness and numerical efficiency, the decomposition was only applied to the phase field evolution equation. In this study, the spectral tension-compression split proposed by Miehe et al. was used, and it is expressed as:

$$\psi^\pm = \frac{1}{2} \lambda \langle \text{tr}^2(\epsilon_a) \rangle_\pm^2 + \mu \text{tr}[\langle \epsilon_a \rangle_\pm^2] \quad (4)$$

where  $\lambda$  and  $\mu$  are the Lamé parameters.  $\epsilon_a$  is the principal strains and  $\langle \square \rangle_\pm$  is a selective operator:  $\langle \square \rangle_\pm = (\square \pm |\square|)/2$ . The history field parameter  $H$  was introduced to meet the damage irreversible condition. The crack driving force is written as:

$$H = \max_{\tau \in [0, t]} \psi_0^+(\tau) \quad (5)$$

where  $t$  is the total time and  $\tau$  is the current time. According to Eq. (2) and Eq. (5), the variation of the internal potential energy  $W_{\text{int}}$  and the external potential energy  $W_{\text{ext}}$  are expressed as:

$$\delta W_{\text{int}} = \int_{\Omega} \sigma \delta \epsilon d\Omega + \int_{\Omega} \left[ \frac{G_c \phi}{l} + 2 \left( \phi - 1 \right) H \right] \delta \phi d\Omega + \int_{\Omega} G_c l \nabla \phi \delta \nabla \phi d\Omega \quad (6)$$

$$\delta W_{\text{ext}} = \int_{\Omega} \bar{\mathbf{b}} \delta \mathbf{u} d\Omega + \int_{\partial\Omega} \bar{\mathbf{t}} \delta \mathbf{u} d\partial\Omega \quad (7)$$

where  $\sigma$  is the Cauchy stress tensor;  $\bar{\mathbf{b}}$  is the volume forces;  $\bar{\mathbf{t}}$  is the surface force and  $\mathbf{u}$  is the displacement field. The balance of virtual power is expressed as:

$$\delta W_{\text{int}} - \delta W_{\text{ext}} = 0 \quad (8)$$

The above formula must satisfy the arbitrary and kinematically admissible variations of the increments of the displacement field  $\dot{\mathbf{u}}$  and the phase field  $\dot{\phi}$ . The corresponding local balance equations and boundary conditions are written as:

$$\text{div}\sigma + \bar{\mathbf{b}} = 0 \text{ in } \Omega \quad (9)$$

$$\frac{H}{G_c} \left(1 - \phi\right) + \frac{l\Delta\phi}{2} - \frac{\phi}{2l} = 0 \text{ on } \partial\Omega \quad (10)$$

$$\boldsymbol{\sigma} \cdot \mathbf{n} = \bar{\mathbf{t}}_0 \text{ on } \partial\Omega \quad (11)$$

$$\nabla\phi \cdot \mathbf{n} = 0 \text{ on } \partial\Omega \quad (12)$$

Where  $\mathbf{n}$  is the normal vector pointing outward on the boundary  $\partial\Omega$ .

For the CSAMed deposits, the mechanical properties of the interface are lower than that of the particles. On this basis, it can be considered that the fracture toughness of the interface  $G_c^I$  is lower than that of the particles  $G_c^P$ . So, the history field parameter should be divided into interface terms  $H^I$  and particle terms  $H^P$ , it can be expressed as:

$$H = H^I + H^P \quad (13)$$

Then, the crack evolution equation Eq. (10) can be rewritten as:

$$\left(\frac{H^I}{G_c^I} + \frac{H^P}{G_c^P}\right) + \left(1 - \phi\right) + \frac{l\Delta\phi}{2} - \frac{\phi}{2l} = 0 \quad (14)$$

## 2.2. Numerical implement

In the framework of the finite element method, the displacement  $\mathbf{u}$  and the phase field  $\phi$  are discretised according to their nodal values  $\mathbf{u}_i$  and  $\phi_i$ , they are expressed as:

$$\mathbf{u} = \sum_{i=1}^n \mathbf{N}_i^u \mathbf{u}_i \text{ and } \phi = \sum_{i=1}^n N_i \phi_i \quad (15)$$

where  $\mathbf{N}_i$  is the shape function matrix and  $N_i$  is the shape function at the  $i$  nodal point.  $n$  is the total number of nodes per element. The  $\mathbf{N}_i$  of 2D elements is written as:

$$\mathbf{N}_i^u = \begin{bmatrix} N_i & 0 \\ 0 & N_i \end{bmatrix} \quad (16)$$

Then, the corresponding derivatives  $\boldsymbol{\epsilon}$  and  $\nabla\phi$  can be obtained by:

$$\boldsymbol{\epsilon} = \sum_{i=1}^n \mathbf{B}_i^u \mathbf{u}_i \text{ and } \nabla\phi = \sum_{i=1}^n \mathbf{B}_i^\phi \phi_i \quad (17)$$

where  $\mathbf{B}_i^u$  and  $\mathbf{B}_i^\phi$  are the spatial derivative matrices, they are written as:

$$\mathbf{B}_i^u = \begin{bmatrix} \partial N_i / \partial x & 0 \\ 0 & \partial N_i / \partial y \end{bmatrix} \text{ and } \mathbf{B}_i^\phi = \begin{bmatrix} \partial N_i / \partial x \\ \partial N_i / \partial y \end{bmatrix} \quad (18)$$

The residual vectors  $\mathbf{R}_i^u$  and  $\mathbf{R}_i^\phi$  can be obtained by discretizing Eq. (6) and Eq. (7) based on the finite element discretization in Eq. (15) and Eq. (17). In the framework of phase field model for CSAM, they can be expressed as:

$$\mathbf{R}_i^u = \int_{\Omega} (\mathbf{B}_i^u)^T \boldsymbol{\sigma} d\Omega - \int_{\Omega} (\mathbf{N}_i^u)^T \bar{\mathbf{b}} d\Omega - \int_{\partial\Omega} (\mathbf{N}_i^u)^T \bar{\mathbf{t}} d\partial\Omega \quad (19)$$

$$\mathbf{R}_i^\phi = \int_{\Omega} \left\{ -2 \left(1 - \phi\right) \mathbf{N}_i \left(\frac{H^I}{G_c^I} + \frac{H^P}{G_c^P}\right) + \left[\frac{1}{l} \mathbf{N}_i \phi + l (\mathbf{B}_i^\phi)^T \nabla\phi\right] \right\} d\Omega \quad (20)$$

Finally, the corresponding tangent stiffness matrices  $\mathbf{K}_{ij}^{uu}$  and  $\mathbf{K}_{ij}^{\phi\phi}$  can be obtained by taking the first derivative of the residual vectors, they are expressed as:

$$\mathbf{K}_{ij}^{uu} = \int_{\Omega} (\mathbf{B}_i^u)^T \mathbf{C} \mathbf{B}_j^u d\Omega \quad (21)$$

$$\mathbf{K}_{ij}^{\phi\phi} = \int_{\Omega} \left\{ \left[ 2 \left(\frac{H^I}{G_c^I} + \frac{H^P}{G_c^P}\right) + \frac{1}{l} \right] \mathbf{N}_i \mathbf{N}_j + l (\mathbf{B}_i^\phi)^T \mathbf{B}_j^\phi \right\} d\Omega \quad (22)$$

The displacement  $\mathbf{u}$  and the phase field  $\phi$  are solved by the iterative

system of linear equations:

$$\begin{bmatrix} \mathbf{u} \\ \phi \end{bmatrix}_{t+\Delta t} = \begin{bmatrix} \mathbf{u} \\ \phi \end{bmatrix}_t - \begin{bmatrix} \mathbf{K}^{uu} & 0 \\ 0 & \mathbf{K}^{\phi\phi} \end{bmatrix}_t^{-1} \begin{bmatrix} \mathbf{R}_u \\ \mathbf{R}_\phi \end{bmatrix}_t \quad (23)$$

The phase field governing equations are solved by the monolithic scheme. According to the previous work [44], the Broyden-Fletcher-Goldfarb-Shanno quasi-Newton algorithm was used to improve the numerical efficiency. In this model, the strain energy density was decomposed into interface and particle terms, the phase field crack driving force was calculated based on different fracture toughnesses. Then, the effect of different interfacial bonding properties on CSAMed deposits can be studied.

## 3. CSAMed deposits model

### 3.1. Deposition process simulation

A 2D Lagrangian method was used to simulate the cold spraying deposition process in Abaqus software. The isotropic Johnson-Cook (J-C) plasticity was used to characterise the plastic behaviour of particles and substrate. The J-C plasticity model is expressed as:

$$\begin{cases} \sigma_y = (A + B\alpha^n)(1 + C \ln(\dot{\alpha}/\dot{\alpha}_0))(1 - T^{*m}) \\ T^* = \frac{(T - T_0)}{T_m - T_0} \end{cases} \quad (24)$$

where  $A$ ,  $B$ ,  $C$ ,  $m$  and  $n$  are material parameters;  $\dot{\alpha}$  is the equivalent plastic strain rate;  $\dot{\alpha}_0$  is the reference strain rate;  $T$  is temperature;  $T_0$  is the room temperature and  $T_m$  is the melt temperature. Pure 6061 aluminium (Al) was used as the particle and substrate materials due to its common applications in CSAM studies. Its mechanical properties have been widely investigated in previous literatures [3,13,15,16,21,23]. The material parameters of 6061 Al [45] are listed in Table 1.

The finite element model is shown in Fig. 1. The Python script was developed to generate particles with diameters of 15  $\mu\text{m}$  to 55  $\mu\text{m}$ . The powder sizes are 19  $\mu\text{m}$  (D10), 34  $\mu\text{m}$  (D50) and 50  $\mu\text{m}$  (D90) [23], where D represents the mass fraction. In order to establish the deposition model, 200 particles of different size were generated in a 1000  $\mu\text{m} \times 100 \mu\text{m}$  area. Based on the observations of previous studies [9,32,33], the mesh size of particles and substrate should be under 1/32 of the average particle size, and was therefore set to 1  $\mu\text{m}$ . The number of elements for particles and substrate are 246618 and 123802, respectively. The temperature-displacement explicit solver was used. In this study, two impact velocities of 600 m/s and 800 m/s were used, with the case of 600 m/s being close to critical velocity [7,46,47]. In order to investigate the effect of interfacial fracture toughness on fracture mode, the 800 m/s (higher than critical velocity) deposit with flat particles was simulated as well [48]. The step times of the 600 m/s and the 800 m/s deposition cases were set to  $2 \times 10^{-6}$  s and  $1.4 \times 10^{-6}$  s, respectively. The penalty contact algorithm in tangential behaviour was applied to

**Table 1**  
Material parameters of 6061 Al [45].

Parameters	Value
Density $\rho$ ( $10^3 \text{ kg/m}^3$ )	2.7
Elastic modulus (GPa)	68.9
Poisson's ratio	0.34
Thermal conductivity $\lambda$ ( $\text{W/(m}\cdot\text{K)}$ )	237.2
Specific heat $c$ ( $\text{J/kg}\cdot\text{K}$ )	898.2
Yield constant $A$ (MPa)	148.4
Hardening constant $B$ (MPa)	345.5
Hardening exponent $n$	0.183
Strain rate constant $C$	0.001
Thermal softening exponent $m$	0.895
Melting temperature $T_m$ (K)	916
Reference temperature $T_0$ (K)	298

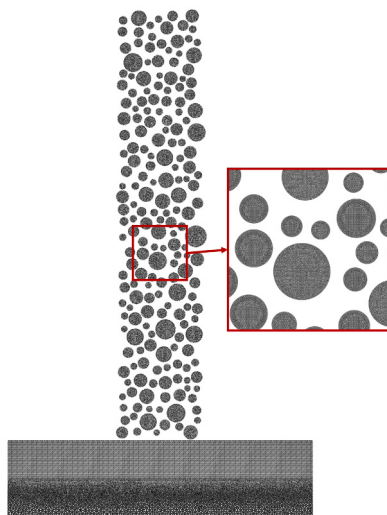


**Fig. 1.** Finite element model of cold spraying deposition process.

the surfaces of all impact particles and the friction coefficient was set to 0.2. The temperature of particles and substrate was set to room temperature of 298 K. All simulations were completed by a computer with an Intel(R) Core(TM) i7-10700 H CPU@ 4.6 GHz processor using 16 cores.

The simulation results of the deposits are shown in Fig. 2. Particles with an impact velocity of 800 m/s deform to a much larger extent than those of 600 m/s. The maximum equivalent plastic strain (PEEQ) for the 600 m/s deposit and the 800 m/s deposit are 4.425 and 5.658, respectively. The larger deformation of particle edge is associated with the high impact velocity, and the equivalent plastic strain of interface is larger than that of particles. The whole analysis cost about 3 h.

### 3.2. Image recognition program

According to the obtained images of deposits, the corresponding finite element models were established. An image recognition program was developed within the Matlab software to identify the boundary and the pores of deposits accurately and efficiently. The pores could be found in the deposits and were recognised to retain the authenticity of the model. The recognition process can be divided into four steps:

- (1) The images of deposits were captured in the area of 80  $\mu\text{m} \times 80 \mu\text{m}$ , as shown in Fig. 3(a).

- (2) The function Im2gray was used to convert the captured RGB image to grayscale image, and it can be expressed as  $I1\_gray = 0.2989 * R + 0.5870 * G + 0.1140 * B$ . Then, the pure black pixels ( $RGB=0$ ) and the pure white pixels ( $RGB=255$ ) were retained from the grayscale image. The spherical filter was used to extend the pure black pixels, and the binary image with the clear boundaries can be obtained. The pure white on the boundaries were introduced into the binary image to represent the pores of deposits, as shown in Fig. 3(b).
- (3) The recognised images were imported into the mesh tool. The pure white (particles) and the pure black (interface) areas were divided into two parts. The different material parameters were set to interface and particles, so the interface was generated into an area with width. The triangular elements were used for meshing the images, as shown in Fig. 3(c).
- (4) The position information of the elements was imported into the HyperMesh software to establish the finite element models for fracture simulation, as shown in Fig. 3(d).

## 4. Results and discussion

### 4.1. Tensile fracture simulation

#### 4.1.1. Parameter settings

The anisotropic tensile fracture behaviour of deposits was investigated by applying loads in two directions: the loading direction parallel to the particle impacting direction ( $0^\circ$ ) and the loading direction perpendicular to the particle impacting direction ( $90^\circ$ ). The boundary conditions and the loading conditions are shown in Fig. 4.

The fracture toughness of particles can be estimated from the wrought 6061 Al, which is about  $10 \text{ kJ/m}^2$  [23]. According to the published experimental results [15,20,23,49,50], the interfacial fracture toughness was estimated to be in the range of about  $10 \text{ J/m}^2$  to  $1 \text{ kJ/m}^2$ . The interfacial bonding properties become better with the increase of the interfacial fracture toughness. The different interfacial fracture toughnesses should be set to investigate the effect of interfacial bonding properties on the anisotropic fracture behaviour of deposits. The three different interfacial fracture toughness cases were used, they are listed in Table 2.

The mechanical parameters of the interface and particles were set to the same values. The Elastic modulus and the Poisson's ratio are listed in Table 1. The transparticular and interparticular fracture modes were considered as the brittle ones. The element size was set to  $0.2 \mu\text{m}$  and the regularization length  $l$  was set to  $0.8 \mu\text{m}$  for the balance of numerical efficiency and convergence [34]. The number of elements for the 600 m/s and the 800 m/s deposits are 197074 and 198055, respectively.

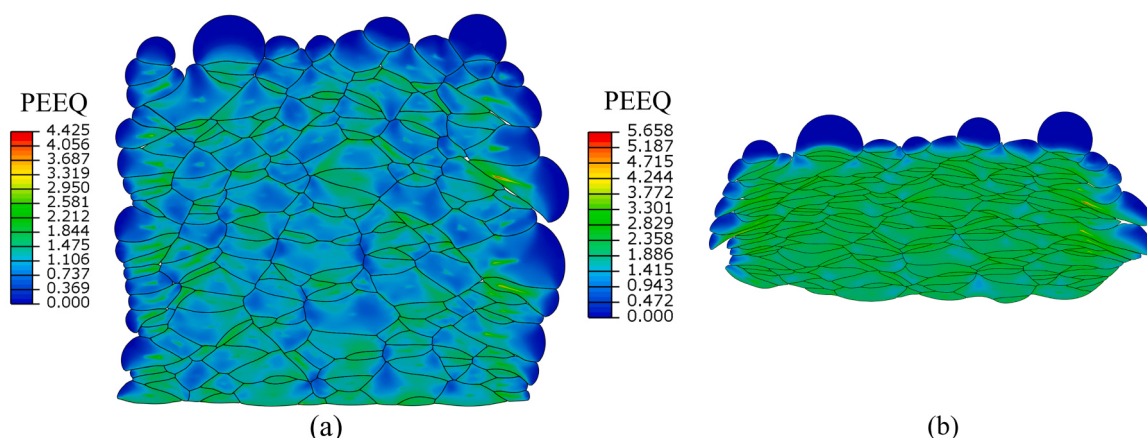


**Fig. 2.** The simulation results of (a) the 600 m/s deposit and (b) the 800 m/s deposit.

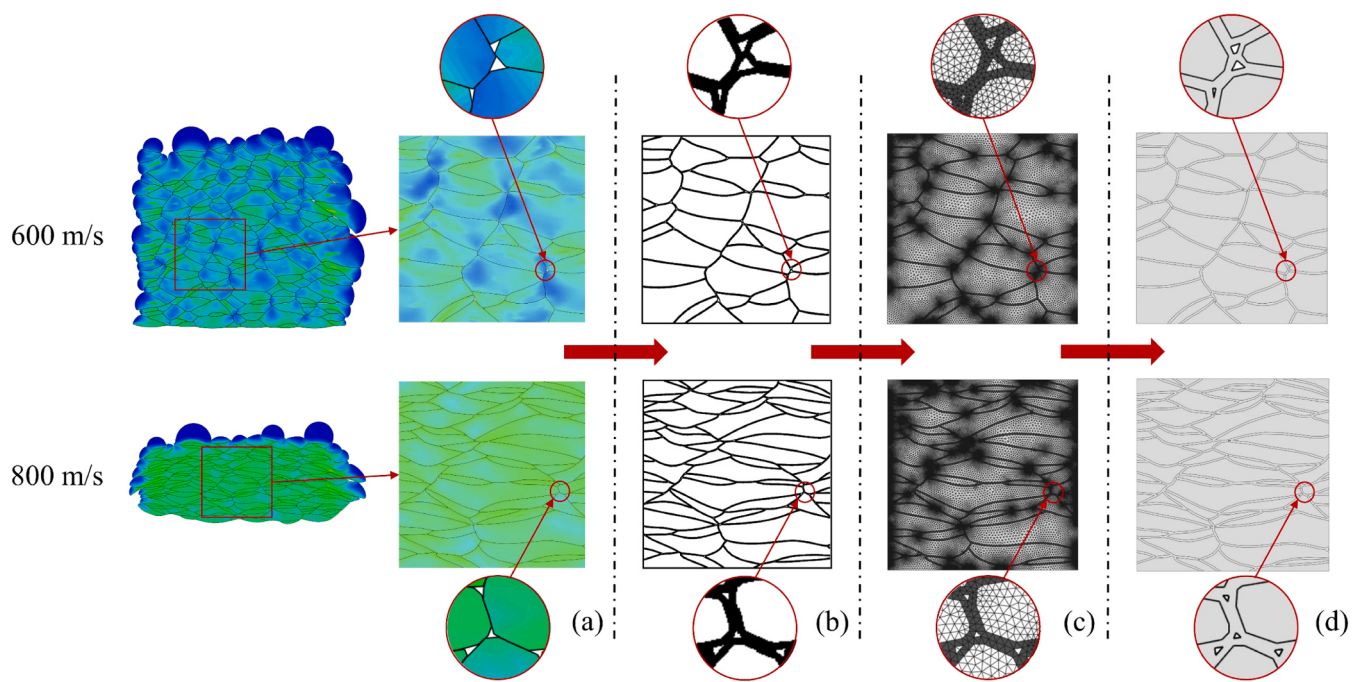


**Fig. 3.** Recognition process: (a) Captured images; (b) Binary images; (c) Meshing; (d) Finite element models for fracture simulation.

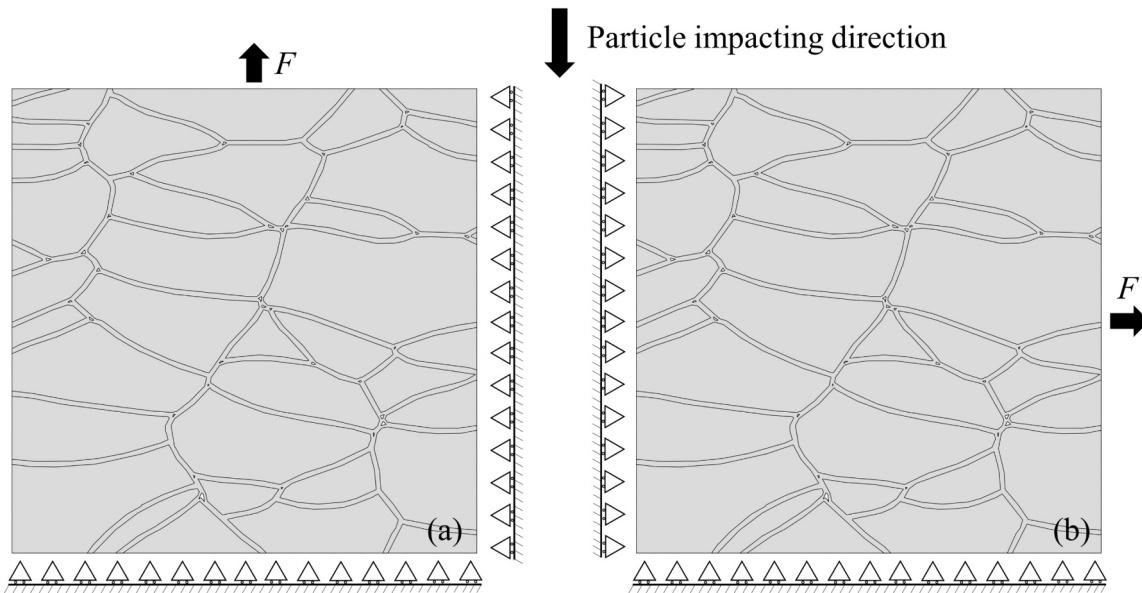


**Fig. 4.** Boundary conditions and loading conditions: (a) 0° and (b) 90°.

**Table 2**

The fracture toughness cases used in this study.

Types	Interface $G_c^I$	Particles $G_c^P$
Case 1	0.01 kJ/m <sup>2</sup>	10 kJ/m <sup>2</sup>
Case 2	0.1 kJ/m <sup>2</sup>	10 kJ/m <sup>2</sup>
Case 3	1 kJ/m <sup>2</sup>	10 kJ/m <sup>2</sup>

#### 4.1.2. Tensile fracture behaviour

For the tensile fracture behaviour of the 600 m/s deposit, the crack paths in 0° and 90° loading directions are shown in Fig. 5. The crack paths of different interfacial fracture toughnesses are similar. The crack initiated from the largest pore relative to the loading direction, and then

propagated along the interface to the edge. The fracture mode is interparticular.

The load-displacement curves of the 600 m/s deposit are shown in Fig. 6. When the interfacial fracture toughness is the same, the fracture anisotropy cannot be observed obviously. The ultimate load and the maximum displacement in 90° loading direction are slightly higher than that in 0° loading direction, which is caused by the slightly longer crack path in 90° loading direction. The longer crack path requires more tensile energy. And the lengths of the crack paths in 0° and 90° loading directions are similar. In this case, the deposit can be considered as the fracture isotropy.

For the tensile fracture behaviour of the 800 m/s deposit, the crack paths in 0° and 90° loading directions are shown in Fig. 7. In 0° loading

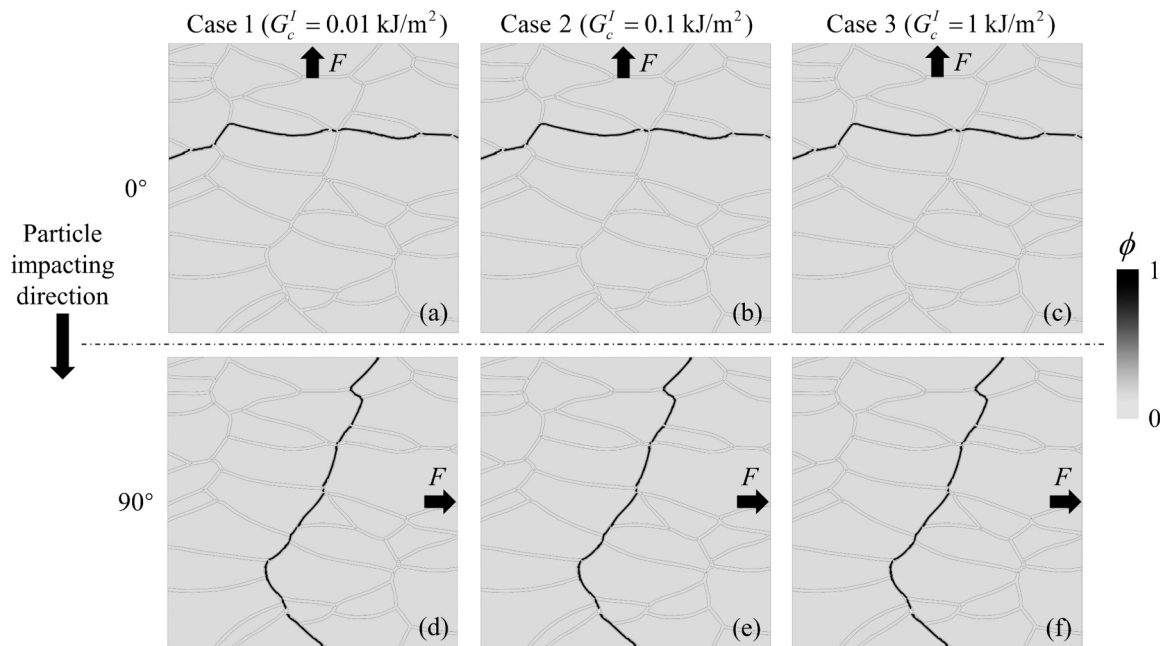


**Fig. 5.** The crack paths of the 600 m/s deposit under different  $G_c^I$ . In  $0^\circ$  loading direction: (a) case 1 (b) case 2 (c) case 3. In  $90^\circ$  loading direction: (d) case 1 (e) case 2 (f) case 3.

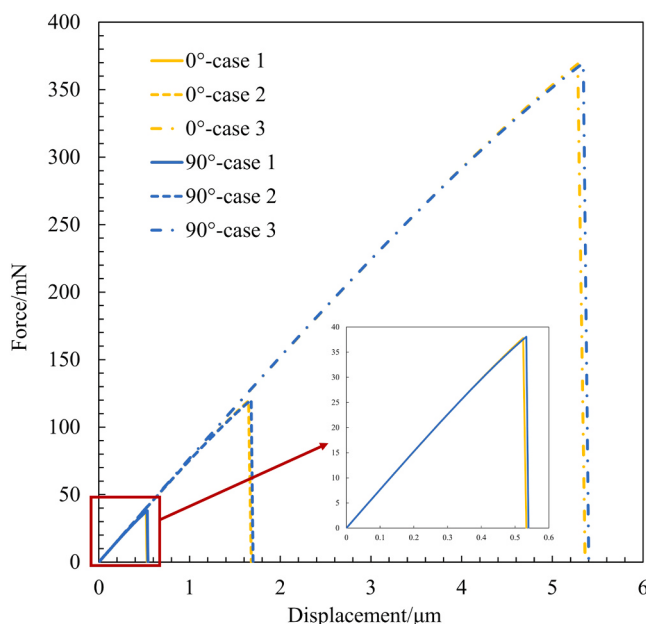


**Fig. 6.** The load-displacement curves of the 600 m/s deposit.

direction, the crack path and the crack length of different interfacial fracture toughnesses are almost the same, and the fracture mode is interparticular. In  $90^\circ$  loading direction, the crack paths of case 1 and case 2 are similar, but quite different from case 3. In case 3, there are two cracks, and the transparticular fracture can be found in the interface with excessive local bending, as shown in Fig. 7(f). The cracks initiated from the largest pore and then almost completely propagated along the interface to the edge. Although there are small scale transparticular cracks, the fracture mode can still be considered as interparticular.

The load-displacement curves of the 800 m/s deposit are shown in Fig. 8. When the same interfacial fracture toughness is used, the ultimate load and the maximum displacement in  $90^\circ$  loading direction are significantly higher than that in  $0^\circ$  loading direction. There is clear

fracture anisotropy with the longer crack length and more tortuous crack path in  $90^\circ$  loading direction. For the deposits with flatter particles in  $90^\circ$  loading direction, the crack growth requires more tensile energy, whether the fracture mode is transparticular (fracture toughness of particles is larger than that of interface) or interparticular (longer crack length). The fracture anisotropy identified in this study matches the experimental results from previous studies [23–26].

The load displacement curves of case 3 are used to compare the fracture behaviour of the 600 m/s deposit and the 800 m/s deposit, as shown in Fig. 9. The ultimate loads of the 600 m/s deposit in  $0^\circ$  and  $90^\circ$  loading directions are 368.9 mN and 369.7 mN, while those of the 800 m/s deposit in  $0^\circ$  and  $90^\circ$  loading directions are 362.3 mN and 403.1 mN. For the deposits produced at different particle velocities with the similar length of crack paths, their ultimate load and maximum displacement are almost the same.

In fact, the bonding properties of particles become better with the increase of the impact velocity. It can be seen that the ultimate load will increase thrice when the interfacial fracture toughness increases by an order, as shown in Fig. 6 and Fig. 8. Compared with the other parameters such as loading directions, crack path length and fracture modes, the interfacial fracture toughness is the most important parameter affecting the bonding property.

#### 4.1.3. Interparticular and transparticular fracture modes

In the case of deposits with flat particles, the fracture mode in  $90^\circ$  loading direction is generally mixed interparticular and transparticular [23]. The interparticular fracture can be regarded as a mixture of mode I and mode II, while the transparticular fracture is almost the mode I, as shown in Fig. 10. The grey lines are the particles and the colored dotted lines are the crack paths. The green and blue lines represent the mode I and mode II of interparticular fracture, respectively. The red line represents the mode I of transparticular fracture.

In order to investigate the effect of tensile and shear strength on the fracture mode of deposits, the different interfacial fracture toughnesses of mode I and mode II were set. According to the previous simulations in Section 4.1.2, the interfacial fracture toughness of mode II is considered to be higher than that of mode I. The modified phase field model was developed to implement the different interfacial fracture toughnesses.

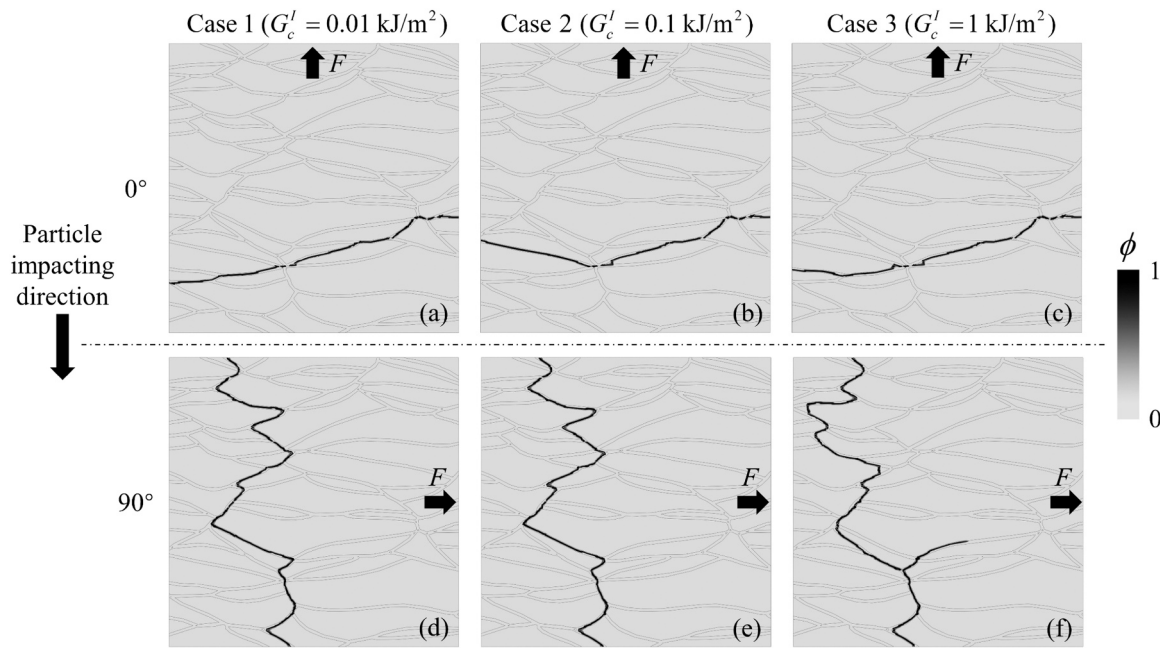


**Fig. 7.** The crack paths of the 800 m/s deposit under different  $G_c^I$ . In  $0^\circ$  loading direction: (a) case 1 (b) case 2 (c) case 3. In  $90^\circ$  loading direction: (d) case 1 (e) case 2 (f) case 3.

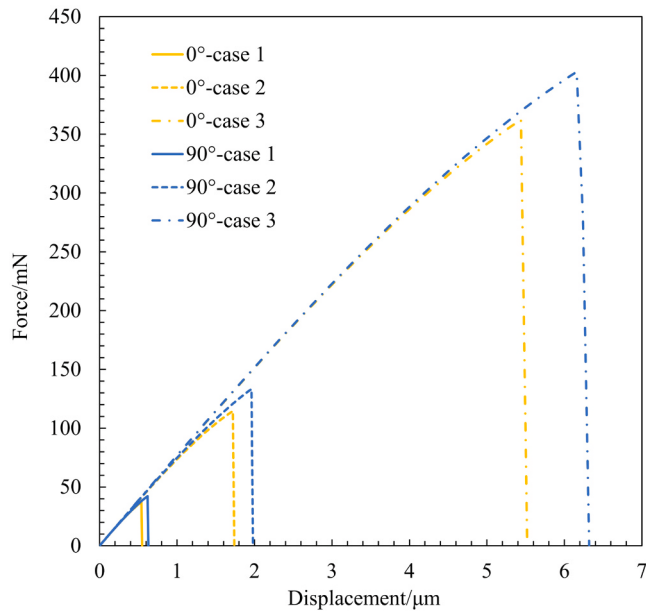


**Fig. 8.** The load-displacement curves of the 800 m/s deposit.

The interfacial history field variable  $H^I$  can be divided into tensile and shearing components [51], and it can be expressed as:

$$H^I = H_I^I + H_H^I \quad (25)$$

where  $H_I^I$  and  $H_H^I$  contribute to the mode I and mode II fracture, respectively. They can be expressed as:

$$\begin{cases} H_I^I = \frac{\lambda}{2} \langle tr^2(\epsilon_a) \rangle_+^2 \\ H_H^I = \mu tr[\langle \epsilon_a \rangle_+^2] \end{cases} \quad (26)$$

The Benzeggagh-Kenane semi-empirical failure criterion [52] was used and the interfacial fracture toughness of mixed mode I/II is

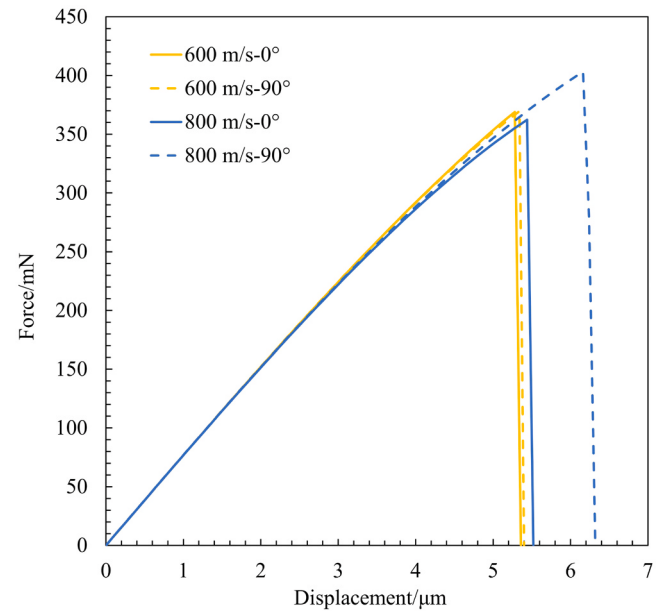


**Fig. 9.** The load-displacement curves of case 3.

expressed as:

$$G'_c = G'_{cl} + \left( G'_{cII} - G'_{cl} \right) \left( \frac{H'_H}{H'} \right)^m \quad (27)$$

where  $G'_{cl}$  and  $G'_{cII}$  are the interfacial fracture toughness relative to mode I and mode II fracture, respectively.  $m$  is the fracture parameter and it was set to 2.6 [53]. Then, the crack evolution equation Eq.(14) can be reformulated as:

$$\left( \frac{H'_I + H'_H}{G'_{cl} + (G'_{cII} - G'_{cl}) (H'_H / H')^m + H'_P} \right) \left( 1 - \phi \right) + \frac{l\Delta\phi}{2} - \frac{\phi}{2l} = 0 \quad (28)$$

In three different cases, the interfacial fracture toughness  $G'_{cl}$  was

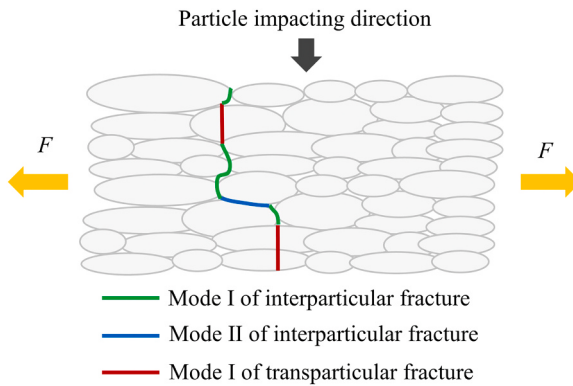


**Fig. 10.** Fracture modes of deposits in 90° loading direction.

fixed and set to 1 kJ/m<sup>2</sup>, while three larger values for interfacial fracture toughness  $G_{cl}^I$  were employed. The modified fracture toughness cases are listed in [Table 3](#).

Modelling focused on the 800 m/s deposit, and the crack paths under different  $G_{cl}^I$  are shown in [Fig. 11](#). In 0° loading direction, the crack path in [Fig. 11\(a\)](#) is similar to that in [Fig. 7\(c\)](#). In [Fig. 11\(b\)](#) and [Fig. 11\(c\)](#), the included angle between the crack propagation direction and the tensile direction is almost 90°. The crack in each case propagated along the interface and the fracture mode is interparticular. In 90° loading direction, the crack path in [Fig. 11\(d\)](#), [Fig. 11\(e\)](#) and [Fig. 11\(f\)](#) is significantly different from that in [Fig. 7\(f\)](#). As the  $G_{cl}^I$  increases, there are more transparticular cracks, less mode II fracture, shorter and smoother crack path. For the tensile fracture simulation, each analysis cost about 2 h.

The load-displacement curves under different  $G_{cl}^I$  are shown in [Fig. 12](#). The ultimate loads of each case in 0° loading direction are 435 mN, 490.2 mN and 540.6 mN. The ultimate loads of each case in 90° loading direction are 483.6 mN, 549 mN and 603.6 mN. For each case, the ultimate loads in 90° loading direction are 11.2%, 12% and 11.7% higher than that in 0° loading direction, respectively. Under different  $G_{cl}^I$ , the fracture anisotropy remains almost constant, but the crack path changes a lot. It can be seen that the different interfacial fracture toughnesses of mode II has great effect on the fracture modes.

#### 4.1.4. Comparison with the experiments

The fracture modes predicted in the previous simulations are compared with the experimental results [23]. In 0° loading direction, the predicted crack paths of the 600 m/s deposit and the 800 m/s deposit are shown in [Fig. 13\(a\)](#) and [Fig. 13\(b\)](#), and the fracture mode is interparticular. In [Fig. 13\(c\)](#), the tortuosity of the crack path is consistent with the edges of the particles in fracture surface. This indicates the main fracture mode is interparticular. The predicted crack paths agree with the experimental results.

In 90° loading direction, when  $G_{cl}^I = G_{cl}^I$ , the predicted crack paths of the 600 m/s deposit and the 800 m/s deposit are almost completely interparticular, as shown in [Fig. 14\(a\)](#) and [Fig. 14\(b\)](#). When  $G_{cl}^I < G_{cl}^I$ , the predicted crack path of the 800 m/s deposit is mixed interparticular and transparticular, as shown in [Fig. 14\(c\)](#). In [Fig. 14\(d\)](#), the tortuosity of the crack path does not conform to the shape of the particles in the fracture surface, and some larger pits than those in [Fig. 13\(c\)](#) suggest

**Table 3**  
The modified fracture toughness cases.

Types	Interface $G_{cl}^I$	Interface $G_{cl}^I$	Particles $G_c^P$
Case 1	1 kJ/m <sup>2</sup>	2 kJ/m <sup>2</sup>	10 kJ/m <sup>2</sup>
Case 2	1 kJ/m <sup>2</sup>	3 kJ/m <sup>2</sup>	10 kJ/m <sup>2</sup>
Case 3	1 kJ/m <sup>2</sup>	4 kJ/m <sup>2</sup>	10 kJ/m <sup>2</sup>

that the crack propagates through particles, which relates to a mixed interparticular and transparticular fracture mode. When the interfacial mode II fracture toughness changes, the predicted crack path is consistent with the experimental one in 90° loading direction.

In this study, the comparison between experiments and the proposed phase field model was performed to validate it in the investigation of fracture and complex crack path of the CSAMed deposits. It should be noted that the fracture mode changes under different interfacial fracture toughness. The agreement with the experiment is the result that the simulation settings are consistent with the actual situation.

## 4.2. Fatigue crack growth simulation

### 4.2.1. Fatigue phase field model for CSAMed deposits

In order to investigate the fracture behaviour under cycle loading, the proposed phase field model was extended to simulate the fatigue crack growth. In this framework, the effect of fatigue load is considered by degrading fracture toughness. The  $f(\bar{\theta}(t))$  is the fatigue degradation function and it can be written as:

$$f\left(\bar{\theta}(t)\right) = \left(\frac{2\vartheta_T}{\bar{\theta}(t) + \vartheta_T}\right)^2 \text{ for } \bar{\theta}(t) \geq \vartheta_T \quad (\text{otherwise } f(\bar{\theta}(t)) = 1) \quad (29)$$

where  $\vartheta_T$  is the fatigue threshold parameter and  $\bar{\theta}$  is the cumulative history variable, and they are expressed as:

$$\vartheta_T = \frac{G_c}{12l} \quad (30)$$

$$\bar{\theta}(t) = \int_0^t H(\vartheta \dot{\vartheta}) |\dot{\vartheta}| dt \quad (31)$$

where  $H(\vartheta \dot{\vartheta})$  is the Heaviside function.  $\vartheta$  is evolving during loading and is defined by:

$$\vartheta = (1 - \phi)^2 H \quad (32)$$

The residual vector  $\mathbf{R}_i^\phi$  and the tangent stiffness matrix  $\mathbf{K}_{ij}^{\phi\phi}$  in [Eq.\(20\)](#) and [Eq.\(22\)](#) can be rewritten as:

$$\mathbf{R}_i^\phi = \int_\Omega \left\{ -2(1 - \phi) \mathbf{N}_i \left( \frac{H^I}{f^I G_c^I} + \frac{H^P}{f^P G_c^P} \right) + \left[ \frac{1}{l} \mathbf{N}_i \phi + l(\mathbf{B}_i^\phi)^T \nabla \phi \right] \right\} d\Omega \quad (33)$$

$$\mathbf{K}_{ij}^{\phi\phi} = \int_\Omega \left\{ \left[ 2 \left( \frac{H^I}{f^I G_c^I} + \frac{H^P}{f^P G_c^P} \right) + \frac{1}{l} \right] \mathbf{N}_i \mathbf{N}_j + l(\mathbf{B}_i^\phi)^T \mathbf{B}_j^\phi \right\} d\Omega \quad (34)$$

where  $f^I$  and  $f^P$  are the fatigue degradation functions corresponding to the interface and particle of deposits.

### 4.2.2. Fatigue life and crack path

The fracture toughnesses of the interface and the particle were set to 1 kJ/m<sup>2</sup> and 10 kJ/m<sup>2</sup>, respectively. The same boundary conditions and loading directions as in the previous simulations were followed, as shown in [Fig. 4](#). The maximum load is 150 mN, and the stress ratio R is 0. The crack growth of the 600 m/s deposit under different cycles is shown in [Fig. 15](#). The crack in 0° and 90° loading directions initiated at 195 and 165 cycles, respectively, as shown in [Fig. 15\(a\)](#) and [Fig. 15\(d\)](#). The fatigue crack propagation process is shown in [Fig. 15\(b\)](#) and [Fig. 15\(e\)](#). The crack propagation life in two directions is 55 and 85 cycles, respectively. The crack propagation life in 90° loading direction is 54.5% higher than that in 0° loading direction. The fatigue life in two directions is 250 cycles, as shown in [Fig. 15\(c\)](#) and [Fig. 15\(f\)](#).

The crack growth of the 800 m/s deposit under different cycles is shown in [Fig. 16](#). The cracks in 0° and 90° loading direction initiated at 185 and 235 cycles, as shown in [Fig. 16\(a\)](#) and [Fig. 16\(d\)](#). The fatigue crack propagation process is shown in [Fig. 16\(b\)](#) and [Fig. 16\(e\)](#). The

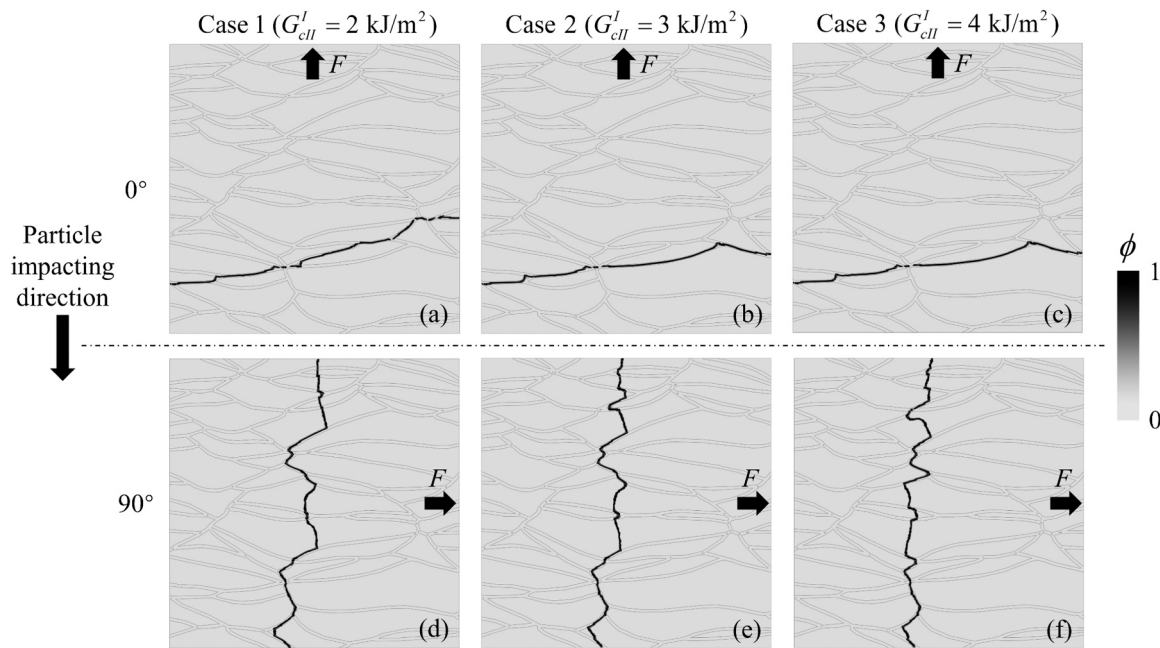


**Fig. 11.** The crack paths of the 800 m/s deposit under different  $G_{cII}^I$ . In  $0^\circ$  loading direction: (a) case 1 (b) case 2 (c) case 3. In  $90^\circ$  loading direction: (d) case 1 (e) case 2 (f) case 3.

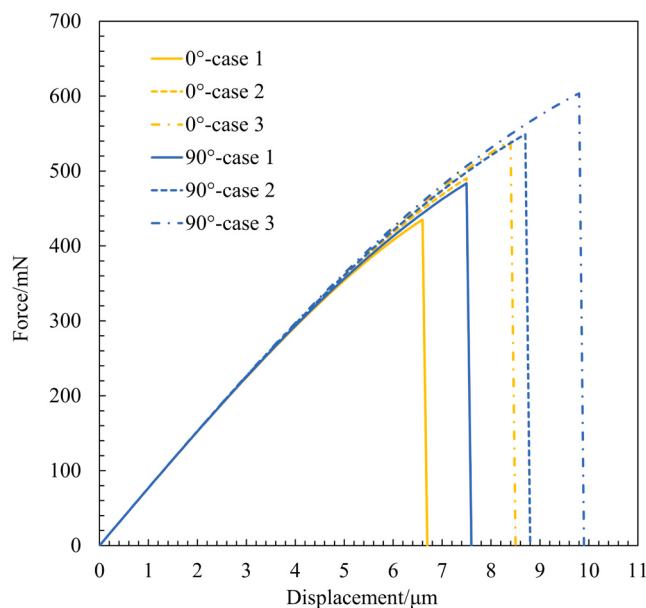


**Fig. 12.** The load-displacement curves under different  $G_{cII}^I$ .

crack propagation life in two directions is 70 and 120 cycles, respectively. The fatigue life in two directions is 255 and 355 cycles, respectively, as shown in Fig. 16(c) and Fig. 16(f). The crack propagation life and fatigue life in  $90^\circ$  loading direction are 71.4% and 39.2% higher than those in  $0^\circ$  loading direction. For the fatigue crack growth simulation, the simulation time ranges from 19 h to 35 h.

In Fig. 15 and Fig. 16, the cracks initiated from the largest pore relative to the loading direction, and then propagated along the interface to the edge. The fracture mode is interparticular, and the crack paths are similar to those in tensile simulation as shown in Fig. 5 and Fig. 7. It can be seen that the fatigue initiation life is related to the area of largest pore in deposits, and the fatigue propagation life is determined by the length of crack path.

## 5. Conclusions

In this study, the Lagrangian method was used to simulate the deposition process. Then, an image recognition program was developed to convert the deposits images into the finite element models for fracture simulation. A phase field model was established to simulate the anisotropic fracture behaviour of CSAMed deposits. The simulated results were compared with the published experimental findings. The main conclusions are as follows:

- (1) The most important parameter affecting the mechanical properties of deposits is the interfacial fracture toughness. The ultimate load of deposits increases thrice when the interfacial fracture toughness increases by an order of magnitude.
- (2) For the deposits with flat particles, the fracture anisotropy is related to the different crack lengths and fracture modes in different loading directions. The ultimate load and fatigue life of the 800 m/s deposit in  $90^\circ$  loading direction are about 11.3% and 39.2% higher than those in  $0^\circ$  loading direction.
- (3) The increase of interfacial fracture toughness of mode II relates to an increased number of transparticular cracks, shorter crack lengths and smoother crack paths.
- (4) The proposed image recognition program can accurately identify the interfaces and the pores of deposits. The proposed phase field model can capture the anisotropic fracture behaviour of deposits, and the predicted crack paths are validated with the published experimental results.

It should be stated that the deposit models developed in 2D are different from ones that would be developed in 3D. Also, the crack path in 2D is a tortuous line, while in 3D would be an uneven surface. Although current models do have some limitations, the fracture behaviour of deposits can be extended to 3D and compared to experimental results. In order to investigate fully the fracture mechanism of deposits, a 3D model will be developed in the near future. The simulation of anisotropic fracture behaviour of CSAMed deposits is a very hard problem. As far as we know, there are few studies focus on this problem. Although this work has some limitations, the results will enrich the

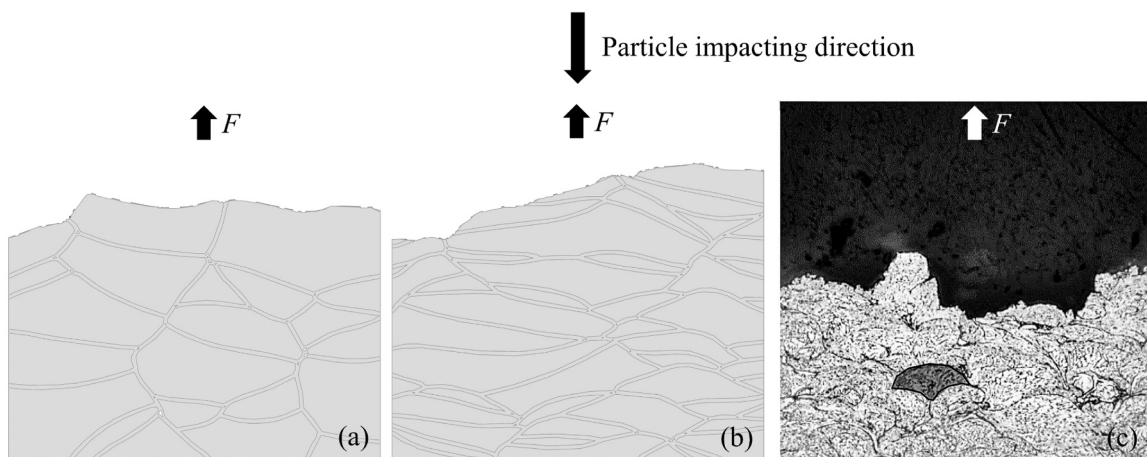


**Fig. 13.** In 0° loading direction: the predicted crack path of (a) the 600 m/s deposit and (b) the 800 m/s deposit; (c) the experimental crack path [23].

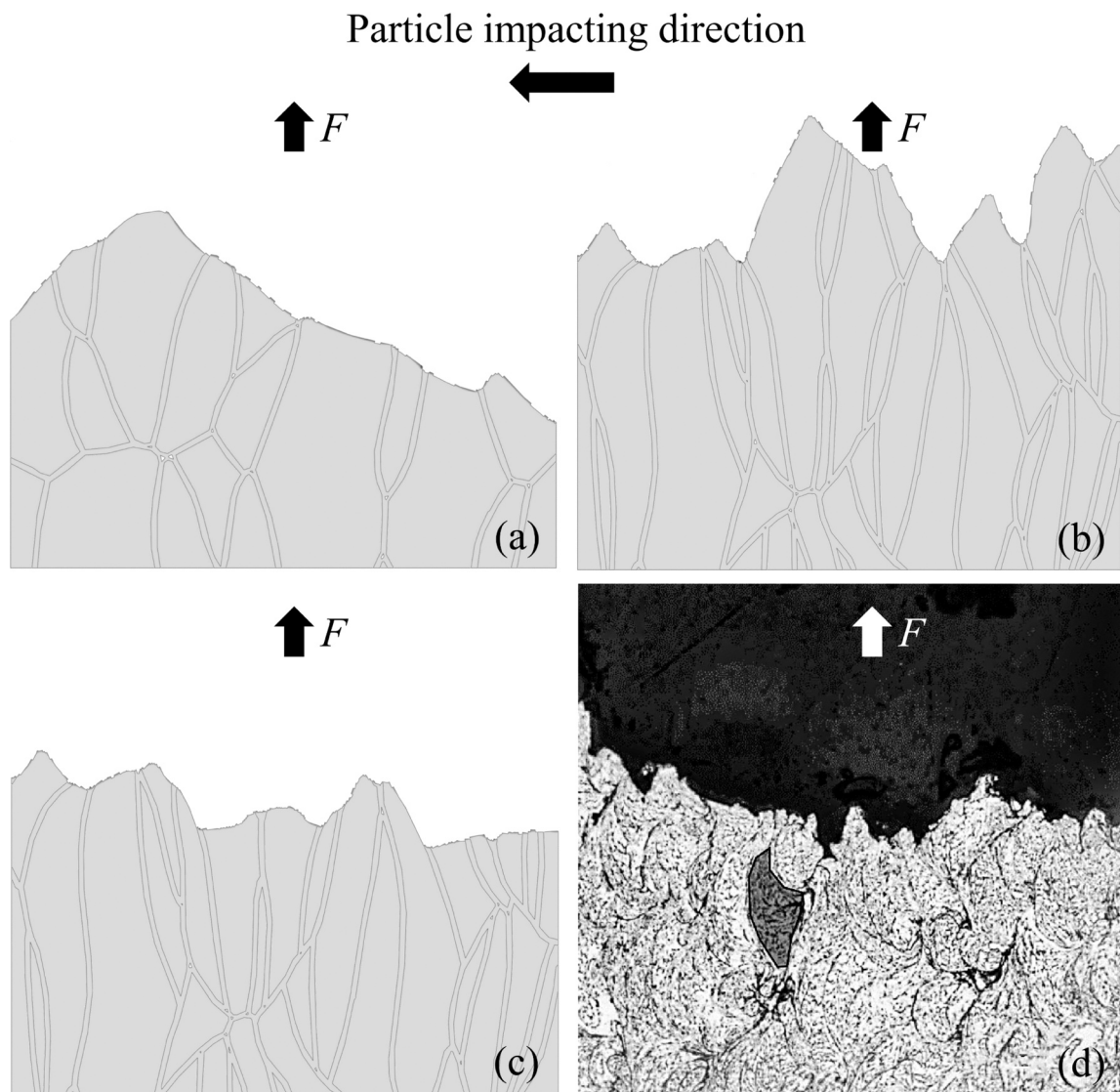


**Fig. 14.** In 90° loading direction: the predicted interparticular crack path of (a) the 600 m/s deposit and (b) the 800 m/s deposit; (c) the predicted mixed crack path of the 800 m/s deposit; (d) the experimental crack path [23].

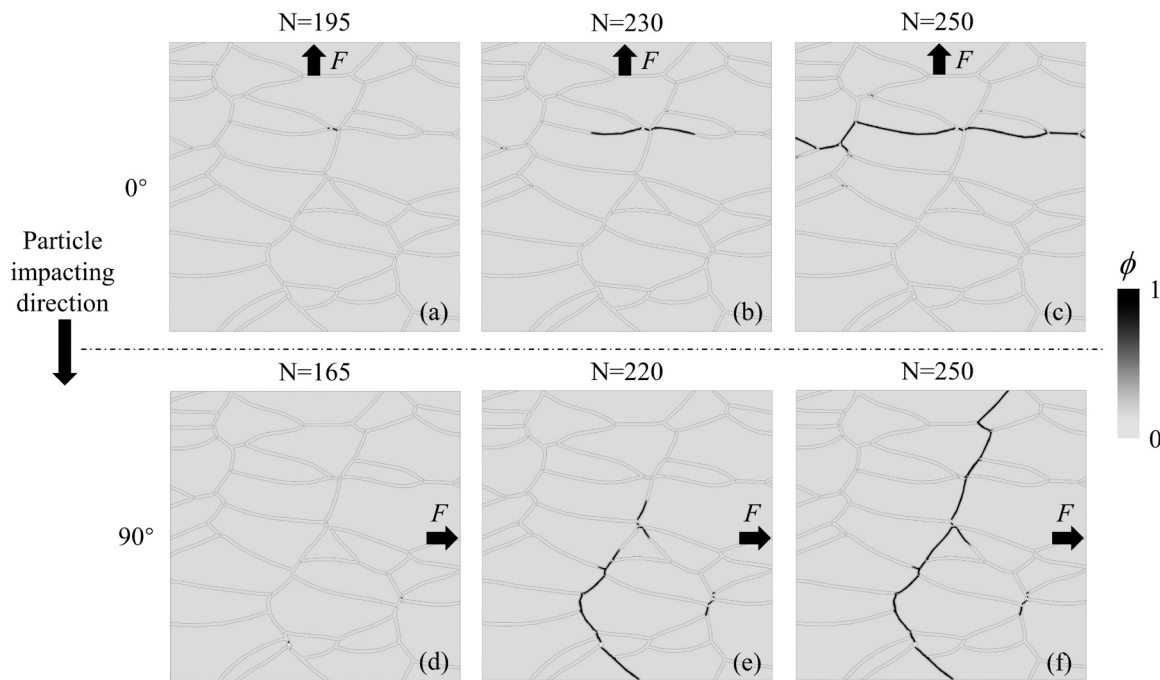


**Fig. 15.** The crack growth of the 600 m/s deposit. In  $0^\circ$  loading direction: (a)  $N = 195$  (b)  $N = 230$  (c)  $N = 250$ . In  $90^\circ$  loading direction: (d)  $N = 165$  (e)  $N = 220$  (f)  $N = 250$ .

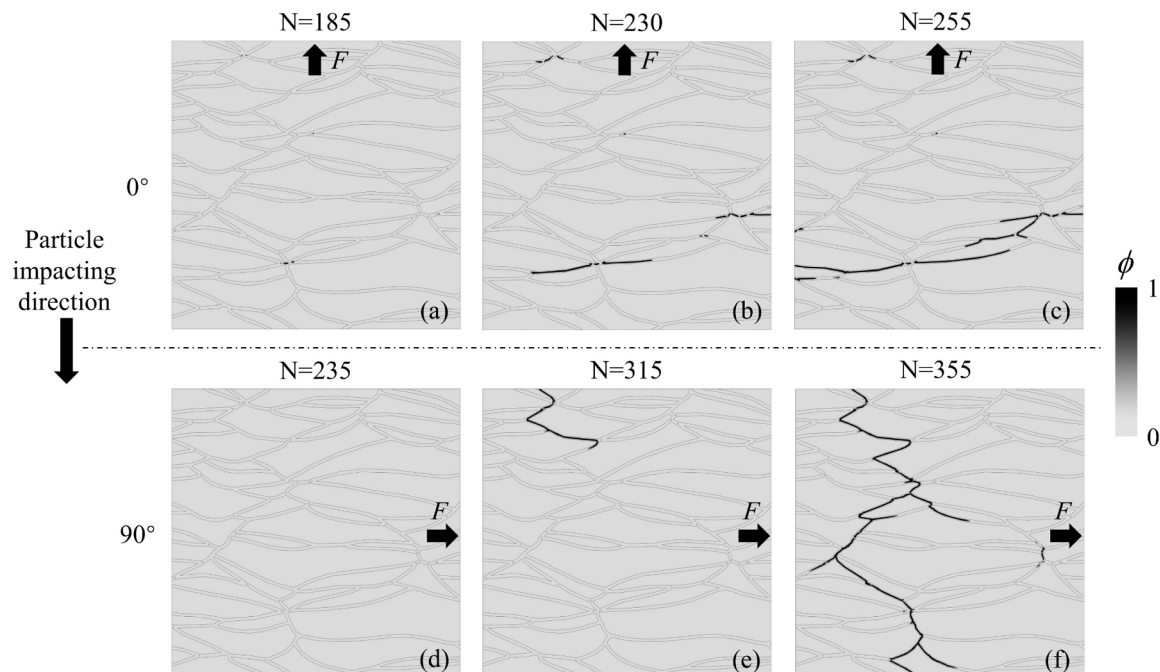


**Fig. 16.** The crack growth of the 800 m/s deposit. In  $0^\circ$  loading direction: (a)  $N = 185$  (b)  $N = 230$  (c)  $N = 255$ . In  $90^\circ$  loading direction: (d)  $N = 235$  (e)  $N = 315$  (f)  $N = 355$ .

theory of deposit fracture behaviour and effectively guide the application of CSAM technology.

#### CRediT authorship contribution statement

**Li Wenyia:** Writing – review & editing, Supervision. **Zhou Linglong:** Validation, Data curation. **Ma Yu E:** Writing – review & editing, Supervision. **Ge Xuanyu:** Writing – original draft, Methodology, Conceptualization.

#### Declaration of Competing Interest

The authors declare that they have no known competing financial interests or personal relationships that could have appeared to influence the work reported in this paper.

#### Data Availability

Data will be made available on request.

## Acknowledgments

This study was financially supported by the National Natural Science Foundation of China under Grant No. 91860128, No. 12032018 and No. 52061135101.

## References

- [1] S. Yin, P. Cavaliere, B. Aldwell, R. Jenkins, H. Liao, W. Li, R. Lupoi, Cold spray additive manufacturing and repair: fundamentals and applications, *Addit. Manuf.* 21 (2018) 628–650.
- [2] C. Huang, A. List, L. Wiehler, M. Schulze, F. Gärtner, T. Klassen, Cold spray deposition of graded Al-SiC composites, *Addit. Manuf.* 59 (2022), 103116.
- [3] Q. Wang, N. Ma, X. Luo, C. Li, Towards better understanding supersonic impact-bonding behavior of cold sprayed 6061-T6 aluminum alloy based on a high-accuracy material model, *Addit. Manuf.* 48 (2021), 102469.
- [4] H. Assadi, H. Kreye, F. Gärtner, T. Klassen, Cold spraying – a materials perspective, *Acta Mater.* 116 (2016) 382–407.
- [5] W. Li, K. Yang, S. Yin, X. Yang, Y. Xu, R. Lupoi, Solid-state additive manufacturing and repairing by cold spraying: a review, *J. Mater. Sci. Technol.* 34 (2018) 440–457.
- [6] W. Li, C. Cao, S. Yin, Solid-state cold spraying of Ti and its alloys: a literature review, *Prog. Mater. Sci.* 110 (2020), 100633.
- [7] H. Assadi, F. Gärtner, T. Stoltzenhoff, H. Kreye, Bonding mechanism in cold gas spraying, *Acta Mater.* 51 (2003) 4379–4394.
- [8] P. Nautiyal, C. Zhang, B. Boesl, A. Agarwal, Interfacial deformation and failure mechanisms at the single-splat length scale revealed in-situ by indentation of cold sprayed aluminum microparticles, *Mater. Sci. Eng. A.* 824 (2021), 141828.
- [9] S. Kumar, B.R. Bodapati, G. Vinay, K. Vamshi Kumar, N.M. Chavan, P. Suresh Babu, A. Jyothirmayi, Estimation of inter-splat bonding and its effect on functional properties of cold sprayed coatings, *Surf. Coat. Technol.* 420 (2021), 127318.
- [10] P. Poza, M.Á. Garrido-Maneiro, Cold-sprayed coatings: microstructure, mechanical properties, and wear behaviour, *Prog. Mater. Sci.* 123 (2022), 100839.
- [11] C.M. Sample, V.K. Champagne, A.T. Nardi, D.A. Lados, Factors governing static properties and fatigue, fatigue crack growth, and fracture mechanisms in cold spray alloys and coatings/repairs: a review, *Addit. Manuf.* 36 (2020), 101371.
- [12] T. Hussain, D.G. McCartney, P.H. Shipway, D. Zhang, Bonding mechanisms in cold spraying: the contributions of metallurgical and mechanical components, *J. Therm. Spray. Technol.* 18 (2009) 364–379.
- [13] M.R. Rokni, C.A. Widener, O.C. Ozdemir, G.A. Crawford, Microstructure and mechanical properties of cold sprayed 6061 Al in As-sprayed and heat treated condition, *Surf. Coat. Technol.* 309 (2017) 641–650.
- [14] S. Bagherifard, J. Kondas, S. Monti, J. Cizek, F. Perego, O. Kovarik, F. Lukac, F. Gaertner, M. Guagliano, Tailoring cold spray additive manufacturing of steel 316 L for static and cyclic load-bearing applications, *Mater. Des.* 203 (2021), 109575.
- [15] A.G. Gavras, D.A. Lados, V.K. Champagne, R.J. Warren, Effects of processing on microstructure evolution and fatigue crack growth mechanisms in cold-spray 6061 aluminum alloy, *Int. J. Fatigue* 110 (2018) 49–62.
- [16] A.G. Gavras, D.A. Lados, V.K. Champagne, R.J. Warren, D. Singh, Small fatigue crack growth mechanisms and interfacial stability in cold-spray 6061 aluminum alloys and coatings, *Metall. Mater. Trans. A* 49 (2018) 6509–6520.
- [17] M.R. Rokni, A.T. Nardi, V.K. Champagne, S.R. Nutt, Effects of preprocessing on multi-direction properties of aluminum alloy cold-spray deposits, *J. Therm. Spray. Technol.* 27 (2018) 818–826.
- [18] K. Yang, W. Li, X. Guo, X. Yang, Y. Xu, Characterizations and anisotropy of cold-spraying additive-manufactured copper bulk, *J. Mater. Sci. Technol.* 34 (2018) 1570–1579.
- [19] P. Nautiyal, C. Zhang, V.K. Champagne, B. Boesl, A. Agarwal, In-situ mechanical investigation of the deformation of splat interfaces in cold-sprayed aluminum alloy, *Mater. Sci. Eng. A.* 737 (2018) 297–309.
- [20] O. Kovarik, J. Siegl, J. Cizek, T. Chraska, J. Kondas, Fracture toughness of cold sprayed pure metals, *J. Therm. Spray. Technol.* 29 (2020) 147–157.
- [21] A. Nourian, T. Schwartz, S. Boese, S. Müftü, Effects of process parameters on cold spray deposition of Al-6061 Alloy, *J. Therm. Spray. Technol.* 31 (2022) 2517–2536.
- [22] C. Huang, M. Arseenko, L. Zhao, Y. Xie, A. Elsenberg, W. Li, F. Gärtner, A. Simar, T. Klassen, Property prediction and crack growth behavior in cold sprayed Cu deposits, *Mater. Des.* 206 (2021), 109826.
- [23] S.E. Julien, A. Nourian-Avval, W. Liang, T. Schwartz, O.C. Ozdemir, S. Müftü, Bulk fracture anisotropy in cold-sprayed Al 6061 deposits, *Eng. Fract. Mech.* 263 (2022), 108301.
- [24] Y. Ren, Nu.H. Tariq, H. Liu, L. Zhao, X. Cui, Y. Shen, J. Wang, T. Xiong, Study of microstructural and mechanical anisotropy of 7075 Al deposits fabricated by cold spray additive manufacturing, *Mater. Des.* 212 (2021), 110271.
- [25] S. Yin, R. Jenkins, X. Yan, R. Lupoi, Microstructure and fracture anisotropy of additively manufactured cold spray copper deposits, *Mater. Sci. Eng. A.* 734 (2018) 67–76.
- [26] K. Yang, W. Li, X. Yang, Y. Xu, Anisotropic response of cold sprayed copper deposits, *Surf. Coat. Technol.* 335 (2018) 219–227.
- [27] A. Fardan, C.C. Berndt, R. Ahmed, Numerical modelling of particle impact and residual stresses in cold sprayed coatings: a review, *Surf. Coat. Technol.* 409 (2021), 126835.
- [28] W. Li, K. Yang, D. Zhang, X. Zhou, Residual stress analysis of cold-sprayed copper coatings by numerical simulation, *J. Therm. Spray. Technol.* 25 (2016) 131–142.
- [29] B. Daneshian, F. Gärtner, H. Assadi, M.V. Vidaller, D. Höche, T. Klassen, Features of ceramic nanoparticle deformation in aerosol deposition explored by molecular dynamics simulation, *Surf. Coat. Technol.* 429 (2022), 127886.
- [30] B. Ren, J. Song, Peridynamic simulation of particles impact and interfacial bonding in cold spray process, *J. Therm. Spray. Technol.* 31 (2022) 1827–1843.
- [31] G. Bae, S. Kumar, S. Yoon, K. Kang, H. Na, H.-J. Kim, C. Lee, Bonding features and associated mechanisms in kinetic sprayed titanium coatings, *Acta Mater.* 57 (2009) 5654–5666.
- [32] G. Vinay, N.M. Chavan, S. Kumar, A. Jyothirmayi, B.R. Bodapati, Improved microstructure and properties of cold sprayed zinc coatings in the as sprayed condition, *Surf. Coat. Technol.* 438 (2022), 128392.
- [33] G. Vinay, S. Kumar, N.M. Chavan, Generalised bonding criteria in cold spraying: revisiting the influence of in-flight powder temperature, *Mater. Sci. Eng. A.* 823 (2021), 141719.
- [34] J.Y. Wu, V.P. Nguyen, C.T. Nguyen, D. Sutula, S. Sinaie, S.P.A. Bordas, Phase-field modeling of fracture, in: S.P.A. Bordas, D.S. Balint (Eds.), *Advances in Applied Mechanics*, Elsevier, 2020, pp. 1–183.
- [35] R. Alessi, M. Ambati, T. Gerasimov, S. Vidoli, L. De Lorenzis, comparison of phase-field models of fracture coupled with plasticity, in: E. Onate, D. Peric, E. de Souza Neto, M. Chiumenti (Eds.), *Advances in Computational Plasticity*, Springer International Publishing, Cham, 2018, pp. 1–21.
- [36] P. Carrara, M. Ambati, R. Alessi, L. De Lorenzis, A framework to model the fatigue behavior of brittle materials based on a variational phase-field approach, *Comput. Methods Appl. Mech. Eng.* 361 (2020), 112731.
- [37] E. Martínez-Pañeda, A. Golahmar, C.F. Niordson, A phase field formulation for hydrogen assisted cracking, *Comput. Methods Appl. Mech. Eng.* 342 (2018) 742–761.
- [38] B. Yin, M. Kaliske, An anisotropic phase-field model based on the equivalent crack surface energy density at finite strain, *Comput. Methods Appl. Mech. Eng.* 369 (2020), 113202.
- [39] G.A. Francfort, J.J. Marigo, Revisiting brittle fracture as an energy minimization problem, *J. Mech. Phys. Solids* 46 (1998) 1319–1342.
- [40] A.A. Griffith, The phenomena of rupture and flow in solids, *Philos. Trans. R. Soc. Lond. Ser. A, Contain. Pap. A Math. Or. Phys. Character* 221 (1921) 163–198.
- [41] J.Y. Wu, Y. Huang, H. Zhou, V.P. Nguyen, Three-dimensional phase-field modeling of mode I + II/III failure in solids, *Comput. Methods Appl. Mech. Eng.* 373 (2021), 113537.
- [42] B. Bourdin, G.A. Francfort, J.J. Marigo, Numerical experiments in revisited brittle fracture, *J. Mech. Phys. Solids* 48 (2000) 797–826.
- [43] M. Ambati, T. Gerasimov, L. De Lorenzis, A review on phase-field models of brittle fracture and a new fast hybrid formulation, *Comput. Mech.* 55 (2015) 383–405.
- [44] X. Ge, Y. Ma, N. Fu, W. Zhang, Z. Wang, A generalized ductile phase field model for fracture behavior of three-dimensional metal structures, *Int. J. Appl. Mech.* (2023) 2350046.
- [45] J. Xie, D. Nélias, H. Walter-Le Berre, K. Ogawa, Y. Ichikawa, Simulation of the cold spray particle deposition process, *J. Tribology* 137 (2015).
- [46] Z. Wang, S. Cai, W. Chen, R.A. Ali, K. Jin, Analysis of critical velocity of cold spray based on machine learning method with feature selection, *J. Therm. Spray. Technol.* 30 (5) (2021) 1213–1225.
- [47] D. John, T. Paul, K. Orikasa, C. Zhang, B. Boesl, A. Agarwal, Engineered aluminum powder microstructure and mechanical properties by heat treatment for optimized cold spray deposition of high-strength coatings, *J. Therm. Spray. Technol.* 31 (8) (2022) 2537–2559.
- [48] X. Wang, F. Feng, M.A. Klecka, M.D. Mordasky, J.K. Garofano, T. El-Wardany, A. Nardi, V.K. Champagne, Characterization and modeling of the bonding process in cold spray additive manufacturing, *Addit. Manuf.* 8 (2015) 149–162.
- [49] W. Xie, A. Alizadeh-Dehkharhane, Q. Chen, V.K. Champagne, X. Wang, A.T. Nardi, S. Kooi, S. Müftü, J.-H. Lee, Dynamics and extreme plasticity of metallic microparticles in supersonic collisions, *Sci. Rep.* 7 (1) (2017) 5073.
- [50] B.C. White, W.A. Story, L.N. Brewer, J.B. Jordon, Fracture mechanics methods for evaluating the adhesion of cold spray deposits, *Eng. Fract. Mech.* 205 (2019) 57–69.
- [51] X. Zhang, S.W. Sloan, C. Vignes, D. Sheng, A modification of the phase-field model for mixed mode crack propagation in rock-like materials, *Comput. Methods Appl. Mech. Eng.* 322 (2017) 123–136.
- [52] M.L. Benzeggagh, M. Kenane, Measurement of mixed-mode delamination fracture toughness of unidirectional glass/epoxy composites with mixed-mode bending apparatus, *Compos. Sci. Technol.* 56 (1996) 439–449.
- [53] S. Liu, Y. Wang, C. Peng, W. Wu, A thermodynamically consistent phase field model for mixed-mode fracture in rock-like materials, *Comput. Methods Appl. Mech. Eng.* 392 (2022), 114642.